Effects of Post-Deposition Annealing Temperature and Time on Physical Properties of Metal-Organic Decomposed Lanthanum Cerium Oxide Thin Film

W. F. Lim, K. Y. Cheong *, and Z. Lockman

Energy Efficient & Sustainable Semiconductor Research Group, School of Materials and Mineral Resources Engineering, Engineering Campus, Universiti Sains Malaysia, 14300 Nibong Tebal, Seberang Perai Selatan, Penang, Malaysia

Tel: +604 599 5259; FAX: +604 594 1011

* Electronic mail: cheong@eng.usm.my

ABSTRACT

Lanthanum cerium oxide ($La_xCe_yO_z$) precursor was prepared using metal-organic decomposition method. The effects of post-deposition annealing temperatures (400-1000 °C) and annealing time (15-120 minutes) in argon ambient on physical properties of the deposited film were investigated. X-ray diffraction was employed to detect presence of phase and crystal orientation in the films. Williamson-Hall plot was used to determine the grain size and microstrains of the film. The grain size increased with the increase of annealing temperature and time while microstrains showed an inverse relationship. High resolution transmission electron microscopy (HRTEM) revealed the formation of three layers on top of the Si substrate. A mechanism, which led to the observation, was proposed.

Keywords: High-k dielectric; lanthanum cerium oxide; metal-organic decomposition; post-deposition annealing; annealing time.

1. Introduction

The continuous downsizing of metal-oxide-semiconductor (MOS) based device dimensions has been the key factor behind the evolution of microelectronics nowadays. The corresponding impact would be the reduction of gate length to 50 nm and gate oxide thickness to 1.5 nm. However, with the advent of gate length technology to 45-22 nm node, ultimate oxide scaling down to EOT of approximately 0.5 nm is required [1]. Although SiO_2 remains the gate oxide material of choice, it is fast approaching its thickness limit. In this regime, unacceptably large leakage currents and reliability concerns accelerate substantial effort in searching for a gate oxide with higher dielectric constant (k) than SiO_2 (k=3.9), allowing the utilization of physically thick gate oxide with electrically equivalent oxide thickness (EOT). Numerous high-k gate oxides, such as Al_2O_3 [2-4], ZrO_2 [5-6], and HfO_2 [7-9] have been employed on Si substrate. Al_2O_3 is also a promising candidate for replacing SiO_2. However, its k value of about 8-10 [] has limited its utilization as a high-k gate oxide. Attention has thus shifted to using HfO_2 and ZrO_2. Both of these oxides possess k values of 20-25 [6-7] yet these k values are insufficient to yield EOT of 0.5 nm. To achieve the ultimate limits of oxide scaling, a new gate oxide with higher k value is required [10-11]. This can be accomplished through the introductory of rare-earth oxides (REOs) [11]. REOs are attractive because there is a compromise between the energy gap and k, so as to combine good insulating properties with potential for oxide scaling. La_2O_3 [12-15], Y_2O_3 [16-19], and CeO_2 [20-22] are the examples of REO, which have been deposited on Si substrate. Among these REOs, La_2O_3 is considered one of the most attractive materials due to its high k (~30) [23], large band gap (5-6 eV) [23-24] and high conduction band offset (2.3 eV) from the Si conduction band [24]. Nevertheless, it is also the most unstable REO because the hygroscopic

nature of La_2O_3 easily turns into $La(OH)_3$ on reaction with ambient water [15, 25-26]. The moisture absorption of La_2O_3 films is partly attributed to the oxygen vacancies in the films [27]. This eventually deteriorates the *k* and electrical properties of La_2O_3 film. In order to alleviate this problem, La_2O_3 is combined with other oxides, such as Al_2O_3, ZrO_2 or HfO_2 to form ternary REO [15, 28-32]. It is anticipated that the addition of La_2O_3 into these oxides improves the *k* of the film because of the high dielectric polarizability of La^{3+} in La_2O_3 [33]. It is reported that they are having a *k* value of 22-27 for $LaAlO_3$ [28] when compared with Al_2O_3 (*k* =8-10) [29] and an increment of *k* value for HfO_2 and ZrO_2 (*k* = 20-25) [6-7] to 38-39 for $La_2Hf_2O_7$ [31] and $La_2Zr_2O_7$ [34].

The beneficial effect of having ternary REO has stemmed the interest of investigating the addition of La_2O_3 to CeO_2. Formation of $La_2Ce_2O_7$ has been reported in previous literatures but it is mainly used for thermal barrier coating due to the fascinating properties, such as low thermal conductivity, high melting point, and thermal expansion match with the underlying substrate that it offers [35-38]. Since there is no pertinent investigation on the employment of $La_xCe_yO_z$ as a gate oxide material, it is of interest to investigate the performance of $La_xCe_yO_z$ for future integration in MOS-based devices. Therefore, the effects of post-deposition annealing temperature (400, 600, 800, and 1000 °C) in argon ambient on the physical properties of metal-organic decomposition (MOD)-derived $La_xCe_yO_z$ spin-coated on n-type Si substrate have been systematically examined in this work.

2. Experimental procedures

The lanthanum cerium oxide precursor was prepared as follows. Lanthanum nitrate (Aldrich) and cerium (III) acetylacetonate hydrate (Aldrich) were used as the starting materials. Initially, small amount of cerium acetylacetonate hydrate powder was dissolved in 3 ml of methanol (J. T. Baker, Analytical grade), followed by an addition of a few drops of acetic acid (J. T. Baker, CMOS grade) to obtain a 0.25 M cerium-containing precursor solution. The mixture was then stirred continuously for 15 min. To achieve a stoichiometric lanthanum cerium oxide, 1:1 molar ratio of La/Ce was maintained. The lanthanum nitrate powder was converted to lanthanum acetylacetonate by dissolving an appropriate amount of the powder in acetylacetone to make up a 0.25 M lanthanum-containing precursor solution. Similarly, this solution was continuous stirring for 15 min and subsequently added to the cerium-containing precursor solution and stirred for another 15 min. After a homogeneous mixture was produced, it was then reflux for 2 h. The resulting lanthanum cerium oxide precursor was allowed to cool prior to spin-coating on a 1-cm^2 cleaned n-type Si (100) substrate. The spinning rate and time were 4000 rpm and 30 s, respectively. Then, the samples were inserted into a horizontal tube furnace for post-deposition annealing at different temperatures (400, 600, 800, and 1000 °C) in argon atmosphere with a heating rate of 5 °C/min for 15 to 120 min. The samples were then cooled down slowly at a rate of 5 °C/min.

In this study, X-ray diffraction (XRD) system (P8 Advan-Bruker) had been used to characterize the presence of phase and orientations of CeO_2 film in the scan range of 25 ° to 60 ° (2θ), using a step time of 71.60 s and step size 2θ of 0.032 °. The X-ray source of Cu-Kα_1 radiation with λ = 1.541 Å was run under a voltage of 40 kV and a current of 40 mA. Williamson-Hall (W-H) plot was applied to calculate the grain size and microstrains contained in

the samples from the XRD line broadening [39]. The oxide thickness and interfacial layer of the samples were determined using high-resolution transmission electron microscopy (HRTEM) (FEI Technai TF-20) operated at 200 kV. The oxide root-mean-square (rms) roughnesses were determined by a non-contact mode atomic force microscopy (AFM) (Nano Navi SPI3800N).

3. Results and Discussion

The XRD patterns of lanthanum cerium oxide ($La_xCe_yO_z$) films annealed at different annealing temperatures (400-1000 °C) are shown in Fig. 1. The film annealed at 400 °C does not reveal any diffraction peaks. As the annealing temperature increases to higher temperatures (600-1000 °C), four diffraction peaks are detected. These peaks are similar to that of pure CeO_2 because $La_xCe_yO_z$ is the solid solution of La_2O_3 in CeO_2 with fluorite type [35]. The XRD patterns of MOD-derived CeO_2 films on Si substrate [22] are included in Fig. 1 for comparison. It is predicted that $La_xCe_yO_z$ peaks produced in this work coincides with the diffraction peaks of CeO_2. Table 1 shows the comparison of diffraction angles of CeO_2 peaks and $La_xCe_yO_z$ peaks obtained in this work. A shift of diffraction angles to lower degrees is observed for all of the $La_xCe_yO_z$ peaks (600-1000 °C) when compared with CeO_2 peaks. This may be attributed to the expansion of the lattice, owing to the formation of CeO_2-La_2O_3/$La_xCe_yO_z$ solid solution [40]. The lattice exhibited expansion because La^{3+} (0.118 nm) had a larger ionic size than Ce^{4+} (0.097 nm) [40].

Previous literatures have reported on XRD patterns of lanthanum cerium oxide with the formula of $La_2Ce_2O_7$. Its XRD patterns were similar to CeO_2 with a small change of lattice

parameter (CeO_2, a =5.4113 Å; $La_2Ce_2O_7$, a =5.5718 Å) [38]. Nevertheless, the ICDD details regarding $La_2Ce_2O_7$ was not available [38]. Based on the reported a value and hkl planes of $La_2Ce_2O_7$, the XRD diffraction angles of $La_2Ce_2O_7$ were deduced using Bragg's law. In addition, the standard XRD patterns of lanthanum cerium oxide with the formula of $Ce_{0.56}La_{0.44}O_{1.78}$ were found in Inorganic Crystal Structure Database (ICSD) with file number of 98-006-2223. It was deduced that current XRD patterns deviated from either $La_2Ce_2O_7$ or $Ce_{0.56}La_{0.44}O_{1.78}$ for less than 5 %. Nevertheless, the XRD patterns were closer to $La_2Ce_2O_7$ due to its smaller percentage of angle deviation and therefore the four diffraction peaks are ascribed to cubic fluorite phases of (200), (220), (311), and (222) planes.

Table 1 shows that as the annealing temperature increases from 600 to 1000 °C, there is a reduction of diffraction angles of the $La_xCe_yO_z$ films, indicating the peak shift to a lower degree. It has been reported that the shift to the lower degree side implied that the lattice parameter increased with the increase of grain size [37]. Williamson-Hall (W-H) plot was used to determine the grain size (D) of the $La_xCe_yO_z$ films from the XRD line broadening, in which the details were discussed in Ref. [41]. The obtained D for the films is shown in Fig. 2 as a function of annealing temperature. As the annealing temperature increases from 600 to 1000 °C, there is an increment in D from 84.10 nm to 94.65 nm. This increasing trend is in agreement with the growth mechanism of thin film, whereby grain size in a film increases when an annealing temperature is increased, owing to the coalescence of small crystallites to form a larger grain [41-43]. Beside the D value, microstrains of the $La_xCe_yO_z$ films were determined using the W-H approach and they are in a decreasing trend with the increasing annealing temperatures, as shown

in Fig. 2. The lowest microstrains obtained at 1000 °C indicates that the presence of oxygen vacancies in this sample is the least [41].

As the annealing temperature increases from 600 to 800 °C, intensity of all $La_xCe_yO_z$ peaks increased (Fig. 1). By further increasing the temperature to 1000 °C, an obvious increment in the intensity of (200) peak was noticed but not for other peaks. This indicated that the $La_xCe_yO_z$ films were preferentially oriented in (200) direction as the annealing temperature increased. Since the highest preferred orientation was obtained at 1000 °C, it is of interest to investigate the effects of extended annealing time onto the characteristics of the films. Apart of 15 minutes, the annealing time was extended further to 30, 60, 90, and 120 minutes. A comparison of the XRD patterns of $La_xCe_yO_z$ films for each annealing time is elucidated in Fig. 3. The intensity of (200) peak is similar when the annealing time increases from 15 to 30 minutes. However, the intensity drops at 60 minutes and continues to decrease in longer annealing time. It is thus generally depicted that the (200)-preferred orientation ceases when annealing time exceeds 30 minutes. W-H approach was also used to determine the D and microstrains of $La_xCe_yO_z$ films. The D increased from 94.65 nm at 15 minutes to 101.37 nm at 30 minutes, 134.90 nm at 60 minutes, 148.21 nm at 90 minutes, and 169.45 nm at 120 minutes (Fig. 4). An inverse trend of microstrains is shown in Fig. 4 as a function of annealing temperature.

AFM analysis revealed the root-mean-square (rms) surface roughnesses of the $La_xCe_yO_z$ films annealed from 400 to 1000 °C. The highest rms surface roughness is perceived by sample annealed at 1000 °C (12.54 nm). The lowest rms roughness (2.07 nm) was obtained at 400 °C, followed by a rougher (3.01 nm) surface at 600 °C and 800 °C (11.43 nm) (Fig. 5). When the

films annealed at different annealing times (15-120 min) at 1000 °C are compared, rms surface roughnesses of the films increase further, as shown in Fig. 6, from 12.54 nm at 15 min to 14.55 nm at 120 min.

Fig. 7 presents the cross sectional dark-field scanning transmission electron microscope (STEM) images of sample annealed at 1000 °C for 15 minutes. It is noticed that three layers labeled as layer 1, layer 2, and layer 3 are formed on top of the Si substrate. Similar observation has been obtained from images focused by high-angle annular dark field (HAADF) detector [Fig. 7 (b)]. Layer 1 of 33 nm was not as dense as layers 2 and 3 [Fig. 7 (a)]. The less dense structure is possibly caused by the presence of oxygen vacancies, which are created when La_2O_3 was dissolved in the CeO_2 matrix. In a fluorite structure of CeO_2, Ce^{4+} cations are eight-fold coordinated with their nearest neighbours and each anion is surrounded tetrahedrally by four cations. When La_2O_3 was dissolved in the CeO_2 matrix, the La^{3+} ions substituted for the Ce^{4+} cations, and formed the solid solution of CeO_2-La_2O_3, which was the $La_xCe_yO_z$ [40]. The formation of solid solution perturbs the symmetry of Ce-O and/or La-O bond, leading to highly disorder oxygen in the lattice and thus promotes oxygen transfer from the bulk to the surface. The enhanced oxygen mobility facilitates the reduction of Ce^{4+} cations, according to Eq. (1) [40] and creates more Ce^{3+} and oxygen vacancies. Meanwhile, the substitution of lower valence of La^{3+} for Ce^{4+} with close ionic radii may also create oxygen vacancies to achieve electroneutrality of the lattice [40].

$$O_o + 2\ Ce_{Ce} = ½\ O_2\ (gas) + V_{ö} + 2\ Cé_{Ce} \quad (1)$$

where, O_o is the lattice oxygen in the CeO_2, Ce_{Ce} is the cerium in the lattice of CeO_2, and $V_{ö}$ is the oxygen vacancy. The released oxygen would diffuse inward and oxidize the Si surface, forming SiO_x layer (layer 3) of approximately 15 nm thick [Fig. 7 (c)-(d)]. Its identity has been proven by the energy dispersive spectroscopy (EDS) analysis, shown by point 4 in HAADF image [Fig. 7 (b)] and spectrum 4 in Table 2. This layer is smooth and appears in amorphous state, as revealed by a larger zoomed STEM image in Fig. 7 (d). Thus, it was not detected in XRD analysis. However, when the region of SiO_x (red dotted square) is zoomed in [Fig. 7 (e)], dot-like nanocrystals are observed. These nanocrystals might be Si nanocrystals. The formation of Si nanocrystals was reported in HfO_2/SiO/HfO_2 with 7 nm and 10 nm thick SiO films, while no nanocrystals were found in HfO_2/4 nm SiO/HfO_2 structures [44]. This indicates that the formation of Si nanocrystals is inhibited when the SiO layer is less than 4 nm [44]. Therefore, it is not surprising to have Si nanocrystals in the SiO_x layer, which was thicker (15 nm) in this work. It was also reported that Si nanocrystals formed in SiO_x film upon annealing at 1000 °C for 30 min were having irregular shapes and the average size of the nanocrystals was reported to be 3 nm [45]. In this work, it is anticipated that the Si nanocrystals formed are having the similar size as the reported one [45] due to the same annealing temperature (1000 °C) and closer annealing time (15 minutes) used. In addition, some portions of SiO_x layer were removed and drifted into the $La_xCe_yO_z$ layer [Fig. 7 (c)]. The observation might be due to the outdiffusion of Si through the $La_xCe_yO_z$ film. These portions would occupy the oxygen vacancies in $La_xCe_yO_z$ layer and bond with La-Ce-O to form La-Si-O, Ce-Si-O, La-Ce-O, and/or La-Ce-Si-O composition, as revealed by EDS analysis at spectra 1-3 (Table 2) and points 1-3 in HAADF image [Fig. 7 (b)]. Fig. 7 (d) depicts that this layer is a mixture of polycrystalline and amorphous structures. These amorphous phases could be La-Si-O, Ce-Si-O, La-Ce-Si-O, or the embedded

SiO_x portions, which contained Si nanocrystals. The polycrystalline structure is contributed by La-Ce-O, which is detectable by the XRD. Besides, a thin layer (11 nm) consisting of La-Ce-Si-O was detected in layer 2, showing a crystalline structure oriented in certain direction [Fig. 7 (d)]. This layer is formed probably due to the interaction between the SiO_x layer and $La_xCe_yO_z$ layer. Since Si nanocrystals are embedded in SiO_x, formation of La-Ce-Si-O should also have Si nanocrystals embedded inside. These Si nanocrystals would drive the La-Ce-Si-O to out-diffuse, as shown by point 3 in Fig. 7 (b).

Fig. 8 depicts the cross-sectional dark-field STEM images of sample annealed at 1000 °C for 120 min. A tremendous increase in the SiO_x thickness (layer 3) to 42 nm was obtained [Fig. 8 (a)]. The increment in SiO_x thickness was caused by the increment in the amount of oxygen to oxidize the Si surface. As the annealing time was extended from 15 min to 120 min, the oxygen mobility was further enhanced and thus more oxygen would be available to form a SiO_x layer. A thicker SiO_x layer is formed during extended annealing time because more Si substrate would be consumed for SiO_x growth. Meanwhile, the removal of SiO_x becomes more aggressive and the removed regions are drifted to the $La_xCe_yO_z$ layer [Fig. 8 (c)]. It has been reported that thermal decomposition of SiO_x to Si and SiO_2 would occur at high temperature annealing (1000-1100 °C) [46] and the increase of SiO_x thickness would lead to the uncontrolled formation of Si nanocrystals at a broader region [44]. This could be seen in Fig. 8 (a) and (b) where nanocrystals seemed to distribute widely in $La_xCe_yO_z$ layer. Although the number of Si nanocrystals increases at the expense of SiO_x amorphous state with the increment of annealing time, the number is still considerably low [45]. This explained why Si crystalline peaks were not detected by XRD [45]. Moreover, the middle layer of La-Ce-Si-O (layer 2) became thicker (16.7 nm) as more

interaction is formed between SiO_x and $La_xCe_yO_z$ layer when the annealing time is prolonged. This layer changed from single crystalline to polycrystalline structure as two different orientations are observed under STEM in Fig. 8 (d). In addition, out-diffusion of the La-Ce-Si-O portions is exaggerated and, eventually, the $La_xCe_yO_z$ layer (layer 1) is no longer continuous due to the wide distribution of Si nanocrystals, which are embedded in SiO_x and La-Ce-Si-O portions. It is noticed that the $La_xCe_yO_z$ layer became denser (25 nm) because most of the oxygen vacancies are occupied by either SiO_x or La-Ce-Si-O bonding. It could be seen from Fig. 8 (d) that a segregation of different structures consisting of a mixture of crystallites and amorphous-like phases is formed. The crystalline structures are contributed by the La-Ce-O, while the amorphous phase might be consisted of La-Ce-Si-O and SiO_x. The wide distribution of Si nanocrystals in 1000 °C annealed film for 120 min is believed to be the main contributor to the largest rms surface roughness obtained in this sample [Fig. 8].

4. Conclusion

In this work, MOD-derived $La_xCe_yO_z$ film was successfully spin-coated on n-type Si (100) substrate. The effects of post-deposition annealing temperatures (400-1000 °C) and time (15-120 min) on physical properties of the films had been investigated and reported. XRD analysis had revealed the presence of cubic fluorite $La_xCe_yO_z$ phases at (200), (220), (311), and (222) diffraction peaks. Williamson-Hall approach was adapted to determine the grain size and microstrains of the films. The microstrains of CeO_2 films were reduced, accompanied by grain growth when annealing temperature and time were increased. High resolution transmission electron microscopy detected that a SiO_x layer (15 nm) was formed between the $La_xCe_yO_z$ film

(33 nm) and Si substrate in the sample annealed at 1000 °C for 15 min. Si nanocrystals were found in the SiO_x layer due to the thermal decomposition of SiO_x at this high temperature annealing. Out-diffusion of Si occurred and caused the drift of SiO_x portions into the $La_xCe_yO_z$ layer, forming a mixture of polycrystalline and amorphous structures. The amorphous structures were contributed by either La-Ce-Si-O, La-Si-O, Ce-Si-O, or the embedded SiO_x portions, which contained Si nanocrystals. Besides, an interaction between the SiO_x and $La_xCe_yO_z$ layers formed an additional La-Ce-Si-O layer (11 nm). The Si nanocrystals embedded in the SiO_x layer would again cause outdiffusion of the La-Ce-Si-O layer. As the annealing time increased to 120 min, a thicker SiO_x layer (42 nm) was formed and more Si nanocrystals were distributed in the layer. This led to increased amount of Si outdiffusion to $La_xCe_yO_z$ layer, forming a non-continuous surface. Furthermore, the interaction between SiO_x and $La_xCe_yO_z$ increased, forming a thicker La-Ce-Si-O layer (16.7 nm). Consequently, more out-diffusion of the La-Ce-Si-O portions into the $La_xCe_yO_z$ layer occurred, occupying the oxygen vacancies and forming a denser structure (25 nm).

ACKNOWLEDGMENTS

The authors would like to acknowledge the financial support of this work by USM Short Term Grant (Grant Number: 6035269). One of the authors (W. F. Lim) would like to acknowledge financial support given by USM-RU-PRGS (8043001) and USM fellowship.

References

[1] K. Henson, H. Bu, M. H. Na, Y. Liang, U. Kwon, S. Krishnan, J. Schaeffer, R. Jha, N. Moumen, R. Carter, C. DeWan, R. Donaton, D. Guo, M. Hargrove, W. He, R. Mo, R. Ramachandran, K. Ramanib, K. Schonenberg, Y. Tsang, X. Wang, M. Gribelyuk, W. Yan, J. Shepard, E. Cartier, M. Frank, E. Harley, R. Arndt, R. Knarr, T. Bailey, B. Zhang, K. Wong, T. Graves-Abe, E. Luckowski, D. –G. Park, V. Narayanan, M. Chudzik, M. Khare, IEDM Tech. Dig. (2008) 645.

[2] P. I. Raisanen, M. Ritala, M. Leskela, J. Mater. Chem. 12 (2002) 1415.

[3] Y. I. Ogita, S. Ohsone, T. Kudoh, F. Sakamoto, Thin Solid Films 516 (2008) 836.

[4] P. Vitanov, A. Harizanova, T. Ivanova, T. Dimitrova, Thin Solid Films 517 (2009) 6327.

[5] P. Vitanov, A. Harizanova, T. Ivanova, C. Trapalis, N. Todorova, Mater. Sci. Eng. B 165 (2009) 178.

[6] W. H. Nam, S. W. Rhee, Chem. Vap. Deposition 10 (2004) 201.

[7] P. S. Lysaght, J. C. Woicik, M. A. Sahiner, B. –H. Lee, R. Jammy, J. Non. Crys. Sol. 354 (2008) 399.

[8] E. Verrelli, D. Tsoukalas, D. Kouvatsos, Phys. Stat. Sol. 5 (2008) 3720.

[9] J. C. Hackley, T. Gougousi, Thin Solid Films 517 (2009) 6576.

[10] M. M. Frank, S. B. Kim, S. L. Brown, J. Bruley, M. Copel, M. Hopstaken, M. Chudzik, V. Narayanan, Microelec. Eng. 86 (2009) 1603.

[11] A. Dimoulas, in: M. Fanciulli, G. Scarel (Eds.): Rare Earth Oxide Thin Films, Topics Applied Physics, vol. 106, Springer-Verlag Berlin Heidelberg, 2007, p.379.

[12] W. M. He, S. Schuetz, R. Solanki, J. Belot, J. McAndrew, Electrochem. Solid-State Lett. 7 (2004) G131.

[13] S. Y. No, D. Eom, C. S. Hwang, H. J. Kim, J. Appl. Phys. 100 (2006) 024111-1.

[14] M. Leskela, K. Kukli, M. Ritala, J. All. Com. 418 (2006) 27.

[15] J. H. Jun, H. J. Kim, D. J. Choi, Ceram. Int. 34 (2008) 957.

[16] K. –H. kwon, C. K. Lee, J. –K. Yang, S. G. Choi, H. J. Chang, H. T. Jeon, H. –H. Park, Microelec. Eng. 85 (2008) 1781.

[17] X. J. Wang, L. D. Zhang, J. P. Zhang, G. He, M. Liu, L. Q. Zhu, Mater. Lett. 62 (2008) 4235.

[18] W. C. Wang, M. badylevich, V. V. Afanasev, A. Stesmans, C. Adelmann, S. V. Elshocht, J. A. Kittl, M. Lukosius, C. Walczyk, C. Wenger, IOP Conf. Series: Mater. Sci. Eng. 8 (2010) 012028-1.

[19] T. A. Minh-Tri, D. Briand, B. Boudart, Y. Guhel, Microelec. Eng. (2010) Article In Press.

[20] M. Wei, K. L. Choy, J. Cryst. Growth 284 (2005) 464.

[21] J. C. Wang, K. C. Chiang, T. F. Lei, C. L. Lee, Electrochem. Solid-State Lett. 7 (2004) E55.

[22] H. J. Quah, K. Y. Cheong, Z. Hassan, Z. Lockman, F. A. Jasni, W. F. Lim, J. Electrochem. Soc. 157 (2010) H6.

[23] M. Suzuki, E. Cartier, M. A. Gribelyuk, N. A. Bojarczuk, M. C. Copel, Appl. Phys. Lett. 77 (2000) 2710.

[24] T. Hattori, T. Yoshida, T. Shiraishi, K. Takahashi, H. Nohira, S. Joumori, K. Nakajima, M. Suzuki, K. Kimura, I. kashiwagi, C. Ohshima, S. Ohmi, H. Iwai, Microelec. Eng. 72 (2004) 283.

[25] Y. Zhao, K. Kita, K. Kyuno, A. Toriumi, Appl. Phys. Lett. 89 (2006) 252905-1.

[26] J. –B. Cheng, A. –D. Li, Q. –Y. Shao, H. –Q. Ling, D. Wu, Y. Wang, Y. –J. Bao, M. Wang, Z. –G. Liu, N. –B. Ming, Appl. Surf. Sci. 233 (2004) 91.

[27] H. J. Kim, J. H. Jun, D. J. Choi, J. Electroceram. 23 (2009) 258.

[28] K. Kukli, M. Ritala, V. Pore, M. Leskela, T. Sajavaara, R. I. Hedge, D. C. Gilmer, P. J. Tobin, A. C. Jones, H. C. Aspinall, Chem. Vap. Deposition 12 (2006) 158.

[29] Y. –P. Liu, W. Lan, Z. –W. He, Y. –Y. Wang, Chin. Phys. Lett. 23 (2006) 2236.

[30] J. G. Gaskell, A. C. Jones, P. R. Chalker, M. Werner, H. C. Aspinall, S. Taylor, P. Taechakumput, P. N. Heys, Chem. Vap. Deposition 13 (2007) 684.

[31] W. He, L. Zhang, D. S. H. Chan, B. J. Cho, IEEE Elec. Dev. Lett. 30 (2009) 623.

[32] W. –S. Kim, S. –K. Park, D. –Y. Moon, B. –W. Kang, H. –D. Kim, J. –W. Park, Thin Solid Films 517 (2009) 3900.

[33] R. D. Shannon, J. Appl. Phys. 73 (1993) 348.

[34] M. Werner, C. Z. Zhao, S. Taylor, P. R. Chalker, K. Black, J. Gaskell, IEEE Proceedings of 16th IPFA, 2009.

[35] X. Q. Cao, R. Vassen, W. Fischer, F. Tietz, W. G. Jungen, D. Stover, Adv. Mater. 15 (2003) 1438.

[36] Y. Wang, H. B. Guo, S. K. Gong, Ceram. Int. 35 (2009) 2639.

[37] J. Y. Li, H. Dai, X. H. Zhong, Y. F. Zhang, X. Q. Cao, Adv. Eng. Mater. 9 (2007) 205.

[38] W. Ma, S. K. Gong, H. B. Xu, X. Q. Cao, Scripta Materialia 54 (2006) 1505.

[39] J. Pelleg, E. Elish, D. Mogilyanski, Metall. Mater. Trans. A36 (2005) 3187.

[40] L. H. Xiao, K. P. Sun, X. L. Xu, Acta Phys. –Chim. Sin. 24 (2008) 2108.

[41] W. F. Lim, K. Y. Cheong, Z. Lockman, J. All. Com. 497 (2010) 195.

[42] I. Petrov, P. B. Barna, I. Hultman, J. E. Greene, J. Vac. Sci. Technol. A 21 (2003) S117.

[43] N. Izu, W. Shin, I. Matsubara, N. Muruyama, Sens. Actuators B 94 (2003) 222.

[44] M. Perego, G. Seguini, C. Wiemer, M. Fanciulli, P. –E. Coulon, C. Bonafos, Nanotech. 21 (2010) 055606-1.

[45] A. Szekeres, T. Nikolova, A. Paneva, A. Cziraki, Gy. Kovacs, I. Lisovskyy, D. Mazunov, I. Indutnyy, P. Shepeliavyi, J. Optoelec. Adv. Mater. 7 (2005) 1383.

[46] W. L. Zang, S. Zang, M. Yang, T. P. Chen, J. Phys. Chem. C 114 (2010) 2414.

Figure Captions

Fig. 1 X-ray diffractographs of $La_xCe_yO_z$ films annealed at different annealing temperatures (400-1000 °C) in comparison with typical CeO_2 film.

Fig. 2 Grain size and microstrains of $La_xCe_yO_z$ films annealed at different annealing temperatures (400-1000 °C).

Fig. 3 X-ray diffractographs of $La_xCe_yO_z$ films annealed at 1000 °C for different annealing times (15-120 minutes).

Fig. 4 Grain size and microstrains of $La_xCe_yO_z$ films annealed at 1000 °C from 15 minutes to 120 minutes.

Fig. 5 Root-mean-square (rms) surface roughnesses of $La_xCe_yO_z$ films annealed at 400-1000 °C.

Fig. 6 A relationship of root-mean-square (rms) surface roughnesses of $La_xCe_yO_z$ films annealed at 1000 °C as a function of annealing time (15-120 minutes).

Fig. 7 Cross sectional high resolution transmission electron microscopy images of samples annealed at 1000 °C for 15 minutes.

Fig. 8 Cross sectional high resolution transmission electron microscopy images of samples annealed at 1000 °C for 120 minutes.

Table Caption

Table 1 A comparison between diffraction angles of CeO_2 and $La_xCe_yO_z$ films annealed at different temperatures (600-1000 °C).

Table 2 Energy dispersive spectroscopy (EDS) analysis of sample annealed at 1000 °C for 15 minutes in weight percentage.

Tables

Table 1 A comparison between diffraction angles of CeO_2 and $La_xCe_yO_z$ films annealed at different temperatures (600-1000 °C).

Plane	CeO_2 (2θ)	600 °C (2θ)	800 °C (2θ)	1000 °C (2θ)
200	33.2040 °	33.1451 °	33.1274 °	33.0803 °
220	47.9545 °	47.9250 °	47.8602 °	47.8307 °
311	54.7964 °	54.7669 °	54.7375 °	54.7021 °
222	56.5761 °	56.5172 °	56.4818 °	56.4523 °

Table 2 Energy dispersive spectroscopy (EDS) analysis of sample annealed at 1000 °C for 15 minutes in weight percentage.

Spectrum	O (wt %)	Si (wt %)	La (wt %)	Ce (wt %)	Total (wt %)
Spectrum 1	20.63	3.79	30.41	45.17	100.00
Spectrum 2	21.08	3.38	35.70	39.84	100.00
Spectrum 3	22.19	3.93	35.58	38.30	100.00
Spectrum 4	54.88	45.12	0.00	0.00	100.00

Figures

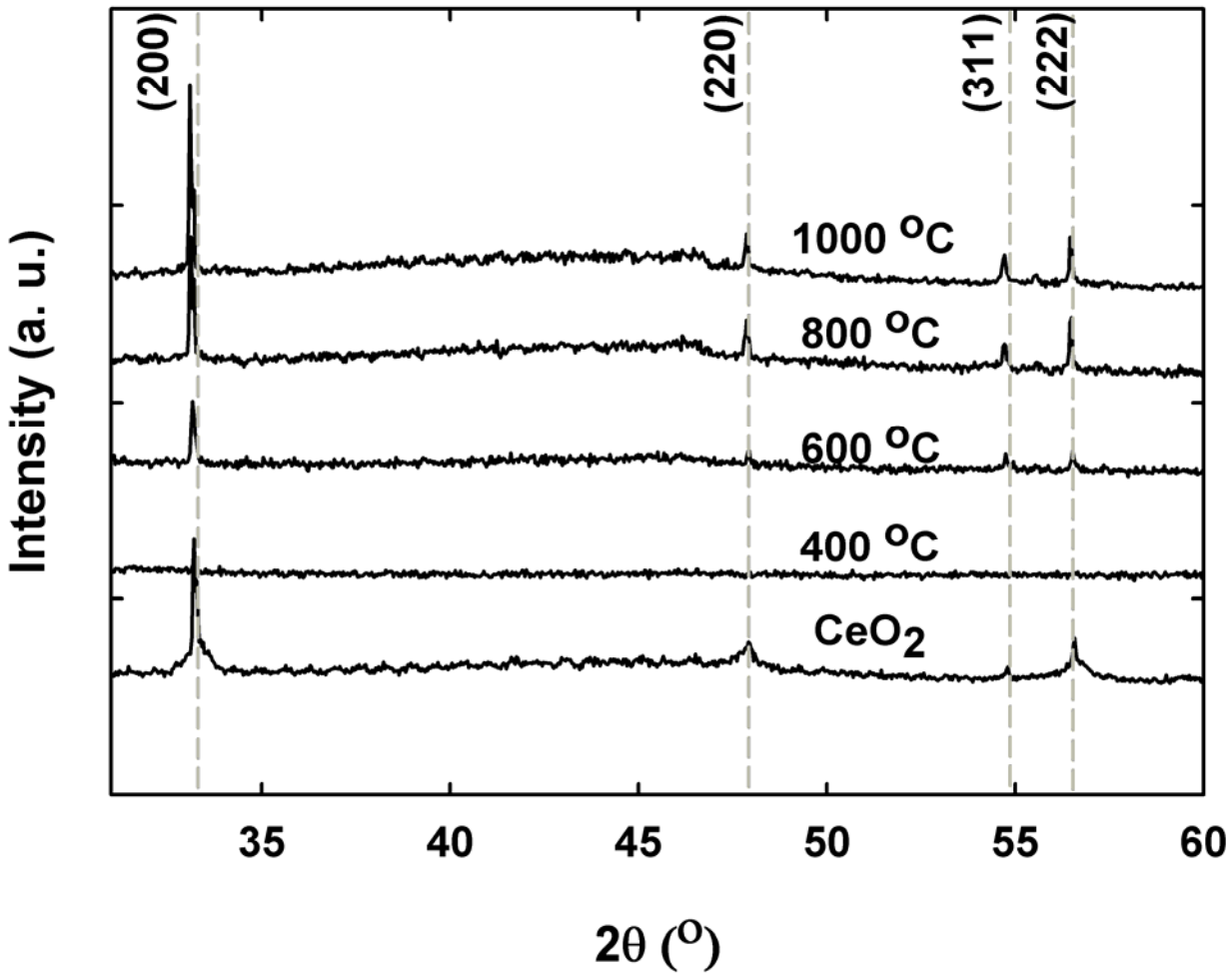

Fig. 1 X-ray diffractographs of $La_xCe_yO_z$ films annealed at different annealing temperatures (400-1000 °C) in comparison with typical CeO_2 film.

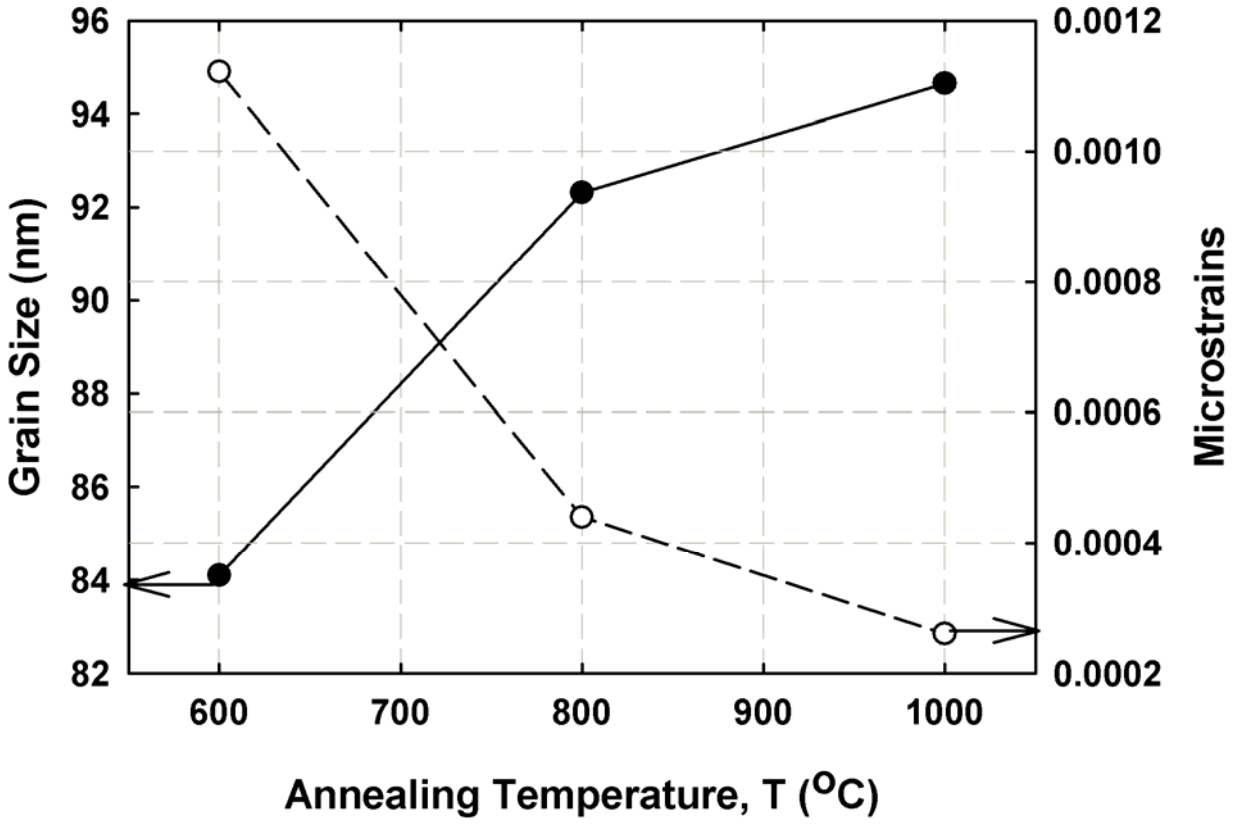

Fig. 2 Grain size and microstrains of $La_xCe_yO_z$ films annealed at different annealing temperatures (400-1000 °C).

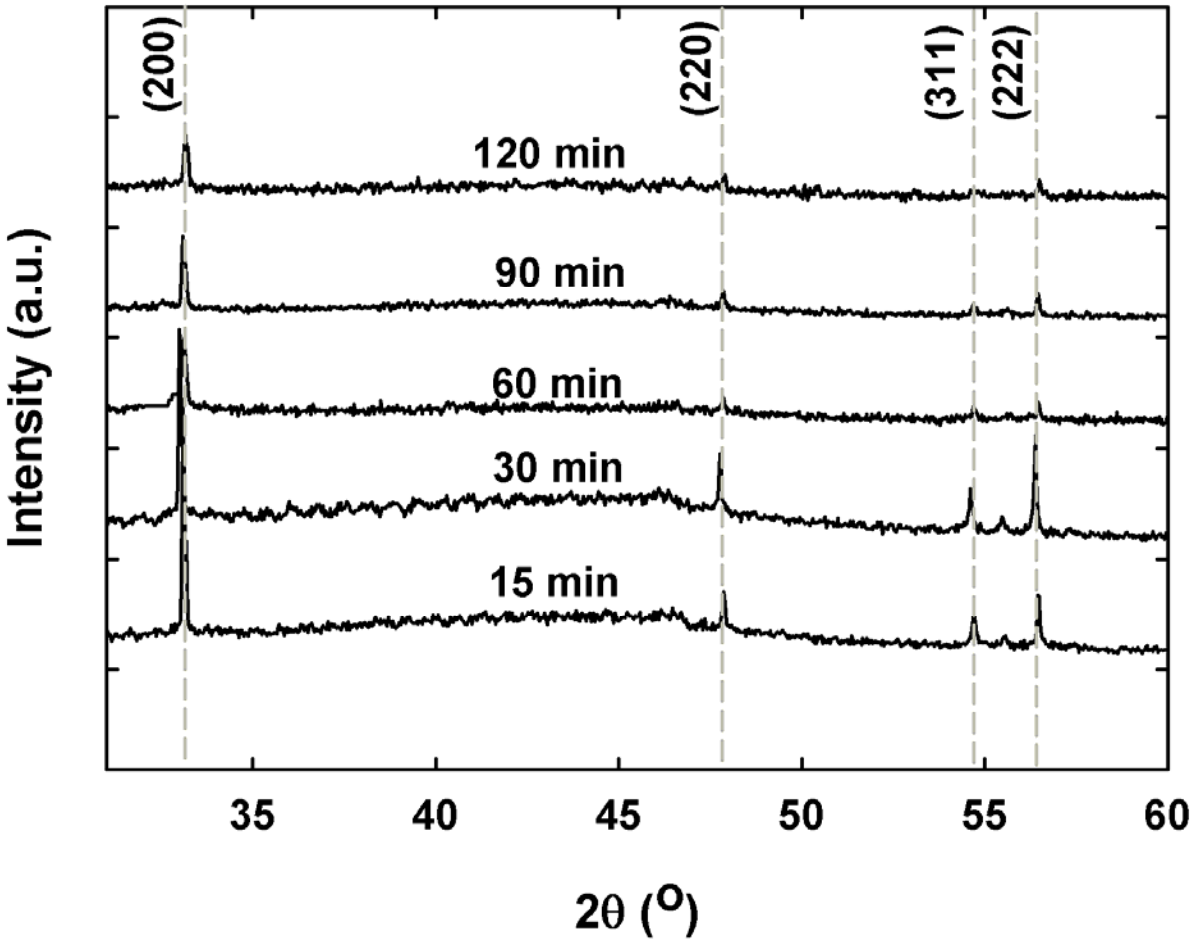

Fig. 3 X-ray diffractographs of $La_xCe_yO_z$ films annealed at 1000 °C for different annealing times (15-120 minutes).

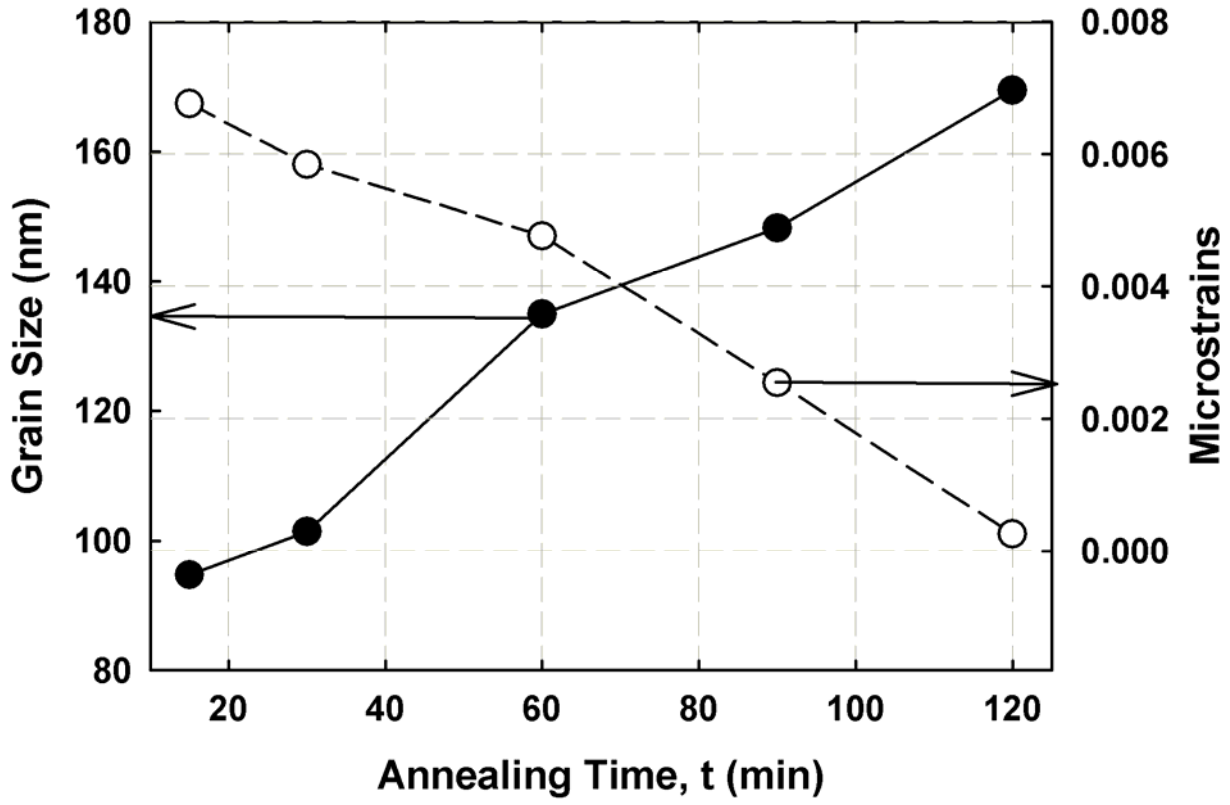

Fig. 4 Grain size and microstrains of $La_xCe_yO_z$ films annealed at 1000 °C from 15 minutes to 120 minutes.

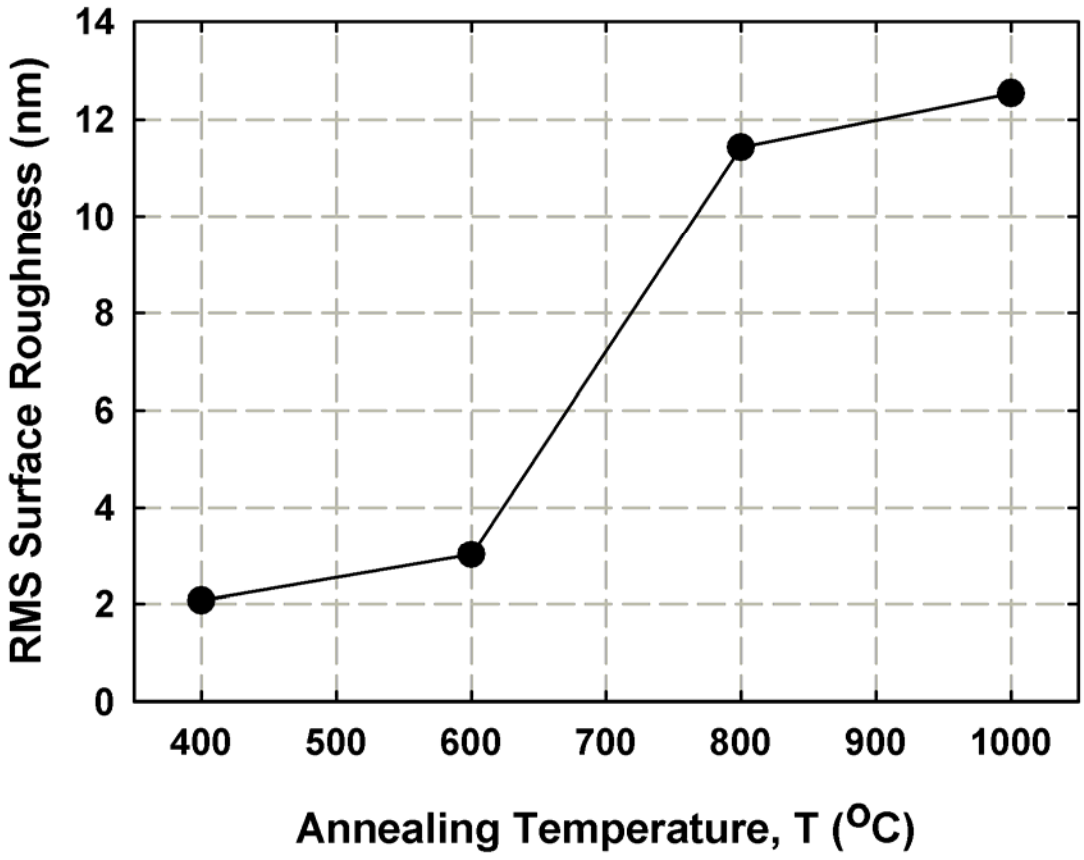

Fig. 5 Root-mean-square (rms) surface roughnesses of $La_xCe_yO_z$ films annealed at 400-1000 °C.

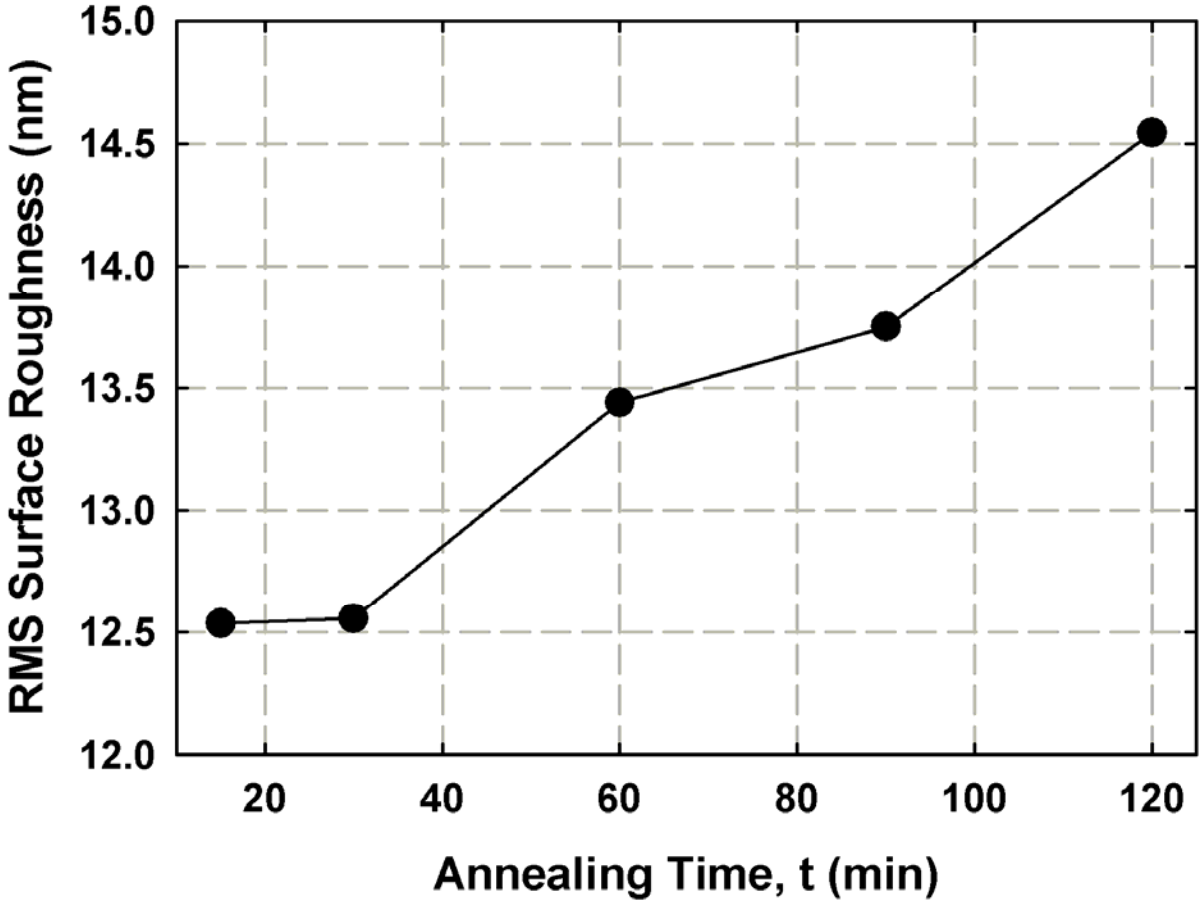

Fig. 6 A relationship of root-mean-square (rms) surface roughnesses of $La_xCe_yO_z$ films annealed at 1000 °C as a function of annealing time (15-120 minutes).

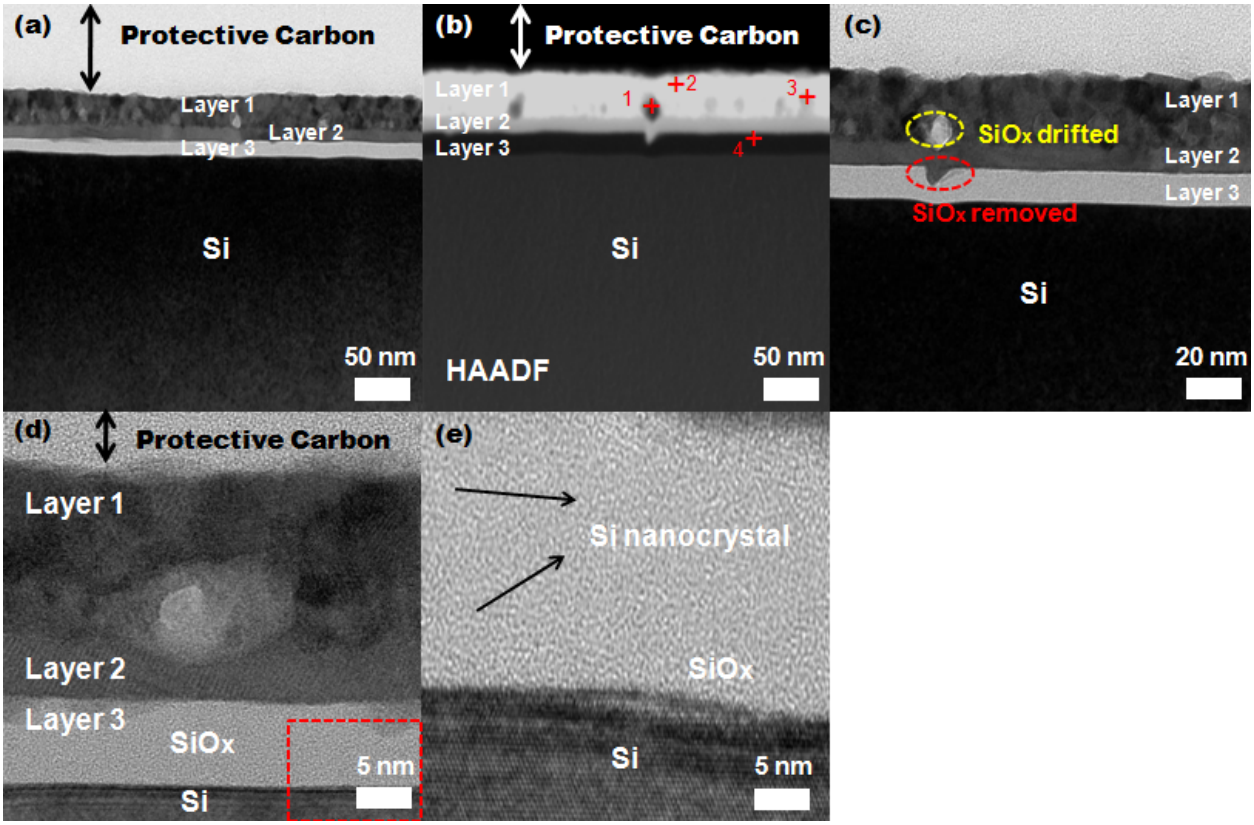

Fig. 7 Cross sectional high resolution transmission electron microscopy images of samples annealed at 1000 °C for 15 minutes.

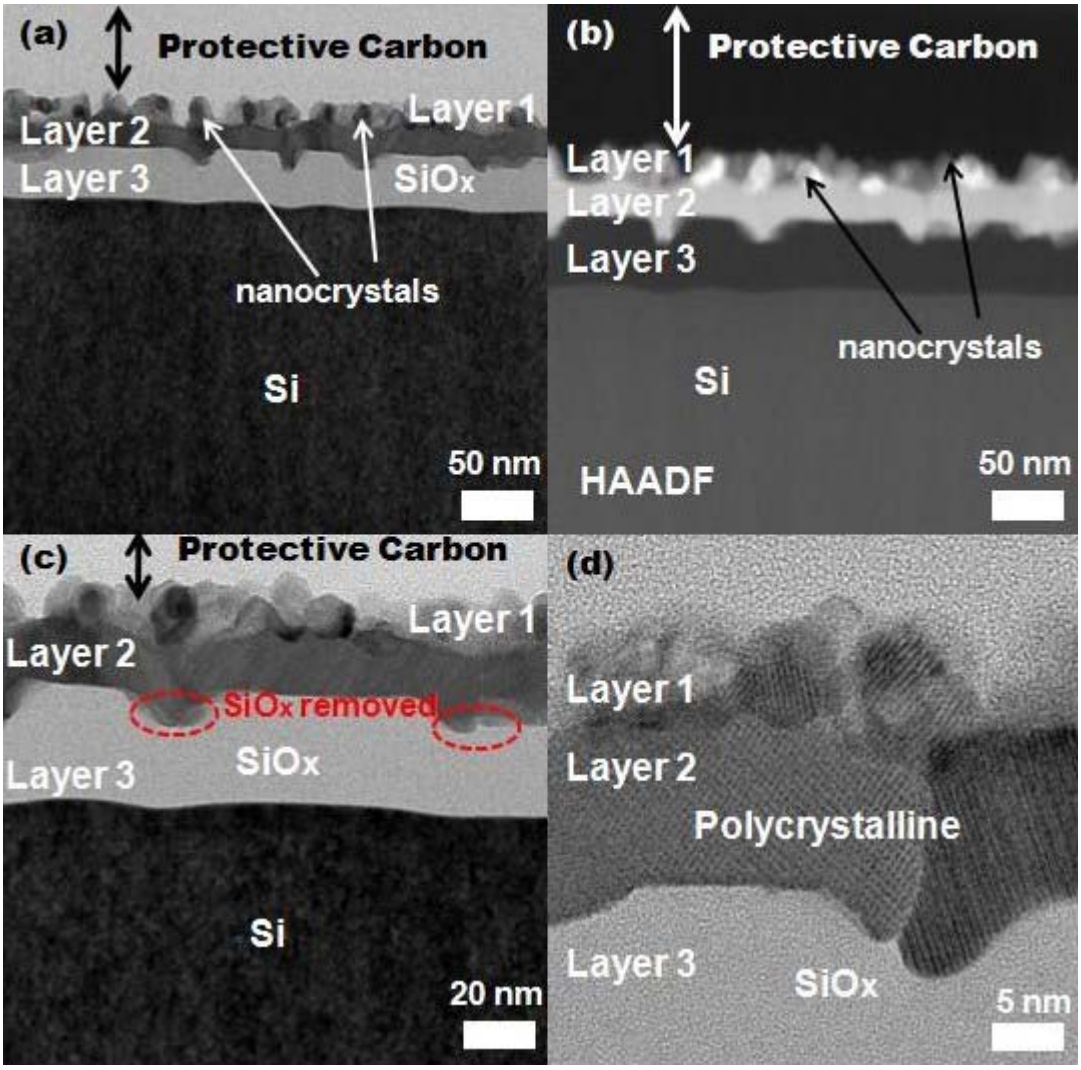

Fig. 8 Cross sectional high resolution transmission electron microscopy images of samples annealed at 1000 °C for 120 minutes.